Engineering Structures 200 (2019) 109736

Contents lists available at ScienceDirect

Engineering Structures

journal homepage: www.elsevier.com/locate/engstruct

Influence of local deck vibrations on the evaluation of the maximum acceleration of a steel-concrete composite bridge for a high-speed railway

Kodai Matsuoka[a,*], Andrea Collina[b], Claudio Somaschini[b], Masamichi Sogabe[c]

[a] Railway Technical Research Institute, Railway Dynamics Division, 2-8-38 Hikari-cho, Kokubunji 185-8540, Tokyo, Japan
[b] Politecnico di Milano, Department of Mechanical Engineering, Via G. La Masa 1, 20152 Milano, Italy
[c] Railway Technical Research Institute, Administration Division, 2-8-38 Hikari-cho, Kokubunji 185-8540, Tokyo, Japan

ARTICLE INFO

Keywords:
High-speed railway
Local deck member vibration
High-order resonance
Railway bridge
Deck acceleration

ABSTRACT

European design standards have established an upper limit on the deck acceleration of the high-speed railway bridges, however the influence of local vibrations of the deck members is rarely considered when modelling the vibrational responses of bridges. To evaluate how the inclusion of local deck vibrations might influence predictions of the maximum acceleration, detailed measurements were taken from a steel-concrete composite box-girder bridge on the Italian high-speed railway, and a numerical model of the system was developed. Deck vibrations were measured during high-speed train passages at the maximum train speed of 374 km/h, and compared against a numerical model of the vehicle-bridge system. This analysis revealed that the maximum deck acceleration is 1.3 times greater than the acceleration of the bridge girders, because of the sixth- and seventh-order resonance between the deck's local vibration modes and the structure with a train running at high speeds over 300 km/h. Moreover, when considering local deck vibrations in the numerical model, we found that the interaction between transient local rail deformations and the vehicle travelling on the rails can increase the acceleration of the deck through resonance.

1. Introduction

The dynamic response of a railway bridge as a high-speed train passes has important effects on safety, passenger comfort, structure fatigue, and concrete cracks. Standards have been established in each country to guide the design, maintenance and running speed as well as to manage the dynamic response of bridges [1–3]. One of the most representative and well-known criteria for the European high-speed railway bridges is the maximum acceleration of the bridge deck as trains pass [4]. This criterion is intended to prevent instability of the ballast track that typically forms European high-speed rails. Eurocode, which is the current international standard, stipulates that the maximum acceleration caused by vibrations at frequencies up to 30 Hz should be less than 3.5 m/s^2 [4]. Many researchers have investigated bridge deck acceleration through experimental and numerical analyses [5–8]. A variety of evaluation methods [9,10] and reduction countermeasures [11,12] have been proposed.

On the other hand, ERRI (European Rail Research Institute), which established the maximum acceleration criteria, pointed out in its final report that local deck vibrations may affect the ballast stability of medium- to long-span bridges, even though the global deformation of the bridge girders is typically used for evaluating the acceptable maximum acceleration of a bridge [3]. However, few design solutions or experimental measurements have considered the influence of local vibrations since then. Even now, only vibrations due to global deformation of the girders, which can be measured in terms of lower-order modes, are considered in most of the literature on this subject [5,13–15]. Considering the typical dimensions of the bridge decks, local vibration modes of a box-type girder may occur at frequencies below 30 Hz, as pointed out in the ERRI's final report [3].

Research groups in Japan and China have measured the local vibration modes of deck members in high-speed railway bridges, for the purpose of evaluating acoustic noise [16–18]. A few groups in Europe have reported similar measurements, such as measurements of slab girders [19–21] and one group has made a theoretical investigation of the same system [22].

The present study first reports field measurements of the local deck vibration modes under 30 Hz, to clarify their contribution to the maximum deck acceleration through high-order resonances. Measurements were taken at the Sesia viaduct on the Milan-Turin high-speed railway,

* Corresponding author at: Structural Mechanics in Railway Dynamics Division, 2-8-38, Hikari-cho, Kokubunji-shi, Tokyo 185-8540, Japan.
E-mail addresses: matsuoka.kodai.13@rtri.or.jp (K. Matsuoka), andrea.collina@polimi.it (A. Collina), claudio.somaschini@polimi.it (C. Somaschini), sogabe.masamichi.78@rtri.or.jp (M. Sogabe).

https://doi.org/10.1016/j.engstruct.2019.109736
Received 23 December 2018; Received in revised form 2 October 2019; Accepted 2 October 2019

which has been studied extensively [13,23–29]. The resonances of the global bending modes have been also studied widely, in ambient vibration tests, train passage tests, mode identifications and numerical simulations [13,23–25]. The amount of deck acceleration caused by high-speed train passages exceeding 300 km/h has also been predicted [29]. Even so, the resonance phenomena caused by local vibrational modes from 20 Hz to 30 Hz are poorly understood, insofar as these resonances amplify the deck vibration and contribute to the maximum deck acceleration. High-speed tests with trains crossing the bridge at speeds up to 374 km/h and our analysis of the resulting vibrational modes clarify that the high-order resonances between local deck modes and the arrangement of the axles of passing trains can cause larger accelerations than those that would be predicted by considering only global vibrations. It should be noted that the field tests and primary analysis can be found in the past literature [30] and some numerical simulations and experimental validations can be also found in another Japanese literature [31]. However, in addition to the past reports, this study includes the new measurement data and detailed analyses focusing on the local vibration modes and passing vehicle excitation frequencies.

Another contribution of this study is to clarify an evaluation method for predicting the maximum deck acceleration with numerical computations. We constructed a numerical dynamic model that can precisely reproduce the local deck modes and acceleration responses that we measured in the field. The numerical model considering vehicle-bridge interaction is composed of vehicle, bridge, and the contact models. Several comparative studies based on the constructed numerical model clarify the existence of local excitation effect in which the local deformation of the rails amplifies the axle load variations and greatly influences the predominance of the maximum deck acceleration caused by the high-order local deck resonances. Finally, a method is proposed for setting the maximum rail deformation modes to be considered in the numerical computation for evaluating the deck acceleration up to 30 Hz.

2. Methods

2.1. Bridge for testing

Figs. 1 and 2 give a photograph and blueprints for the Sesia viaduct [30]. This bridge has 15 diaphragms between steel box girders at 3.114 m intervals. The thicknesses of the main girder web and the lower flange are 20 mm and 25 mm to 15 m of both ends of the bridge, and 18 mm and 30 mm over the centre 15.2 m. This study focuses on the precast concrete deck with a width of 13.6 m and averaged thickness of 0.4 m, which is connected by a two-box steel girder with a width of 10.2 m and a height of 3.35 m. As shown in Fig. 2, the concrete deck and the steel girder are connected by shear studs installed on the steel girder upper flange and lateral beams at both girder ends, but there exists some margin between the lateral upper beam, other than the girder ends and the deck. The target concrete deck is expected to lie close to the surrounding simply supported plate.

2.2. Measurement equipment and signal processing

2.2.1. Measurement system

Table 1 and Fig. 3 show the specifications of the measurement equipment we used and the arrangement of the accelerometers that were installed on the bridge, respectively. To measure the structure's acceleration and the train speed during train passages, 10 accelerometers and 2 pairs of photodiode light-detection systems [30,31] were installed, respectively. Six servo type accelerometers, marked as G1-G6, were installed on the upper flanges of the steel girder, as shown in Fig. 3. To measure the sleeper, a piezoelectric accelerometer, marked as S, was installed at the centre of the sleeper in the mid-span of the track bound for Milan. Piezoelectric accelerometers marked D1 to D3 were installed directly on the bottom surface of the concrete deck at the position shown in Fig. 3. Two pairs of laser detection systems were installed with 110 m between them, on utility poles. The detection system consisted of a light projector and a light receiver that projected a beam of light across the track. The signal produced when the light beam is interrupted was used to trigger automatic measurements, estimate the train running speed and to synchronise measured responses. After A / D conversion, the signals obtained from each sensor were recorded in an on-site PC at a sampling frequency of 2 kHz.

2.2.2. Test train

Table 2 shows the specifications of the passing train used for the measurements, an ETR 1000 with 8 cars [30,31]. The weight of this train was adjusted to 120% of full capacity for our tests. The train running speed was gradually increased, up to the maximum speed of 374 km/h. Measurements were recorded with the train travelling over the bridge towards Milan, and the accelerations were recorded during a total of 32 passages.

2.2.3. Signal processing and model identification

The acceleration responses were resampled to 200 Hz and converted into 15 and 30 Hz low-pass filtered (LPF) accelerations with a band-pass filter and pass bands of 0.5–15 and 0.5–30 Hz. The former is used for the analysis of the global vibration of the bridge, and the higher-frequency signal is used for the evaluation of the maximum deck acceleration based on the Eurocode [4].

Residual vibrations after a train had passed were regarded as free vibration responses, and the global and local deck vibration modes of the Sesia viaduct were identified from the accelerometer data. It should be noted that the identified modal characteristics are not those of a complete bridge alone since include interaction effect with the vehicle [13]. Past literature indicated that could exist a time or amplitude dependency for bridge natural frequencies and modal damping ratios [32]. However, the main objective of this research is analysing the local deck vibration, and thus, detailed experimental analysis focusing on these influences will be discussed in the next study. Modal characteristics were identified using the Eigen-Realisation Algorithm (ERA) method [33]. ERA identifies the natural frequency, the modal damping ratio and the shape of the vibration mode through a characteristic matrix. The calculations process the accelerations on the assumption

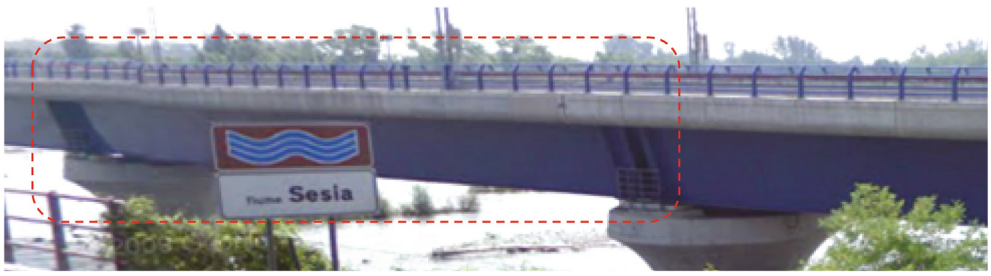

Fig. 1. Picture of the Sesia viaduct [30,31]

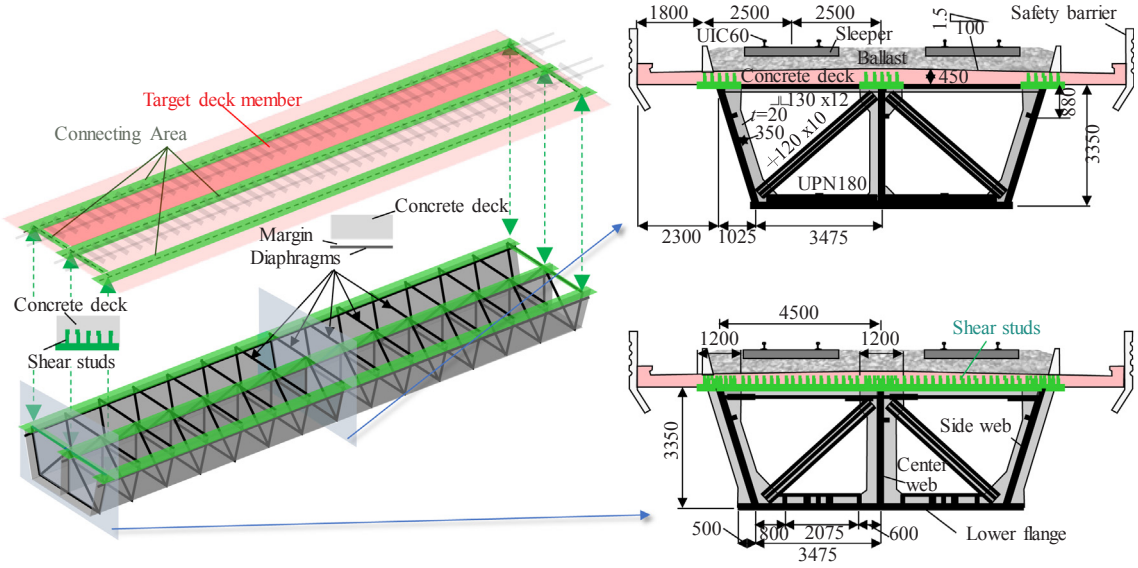

Fig. 2. Structural diagrams of the Sesia viaduct.

Table 1
Specifications of measurement equipment.

Instruments	Model	Specifications
Servo accelerometer for girder	JA-5L15	Freq. range: 0–2000 Hz, Sensitivity: 3.0 V/g
Capacitive accelerometer for slab	141B	Freq. range: 0–300 Hz, Sensitivity: 0.25 V/g
Piezoelectric accelerometer for sleeper	4508	Freq. range: 4–8000 Hz, Sensitivity: 0.1 V/g
Photocell	LS111FA	0, 12 V switching
Data acquisition system	Ni cDAQ-9172 LabVIEW	Sampling: 2 kHz

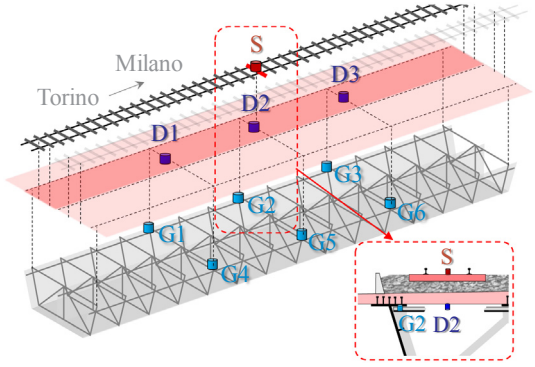

Fig. 3. Arrangement of accelerometers.

Table 2
Specifications of the employed trains.

Type	Wheel load [kN]	Train Speed [km/h]	Measured num.	Direction
ETR1000	Vehicle 1 and 8: 81.8 Vehicle 2 and 7: 76.1 Vehicle 3 and 6: 75.6 Vehicle 4 and 5: 60.7	288–374	32	Torino to Milano

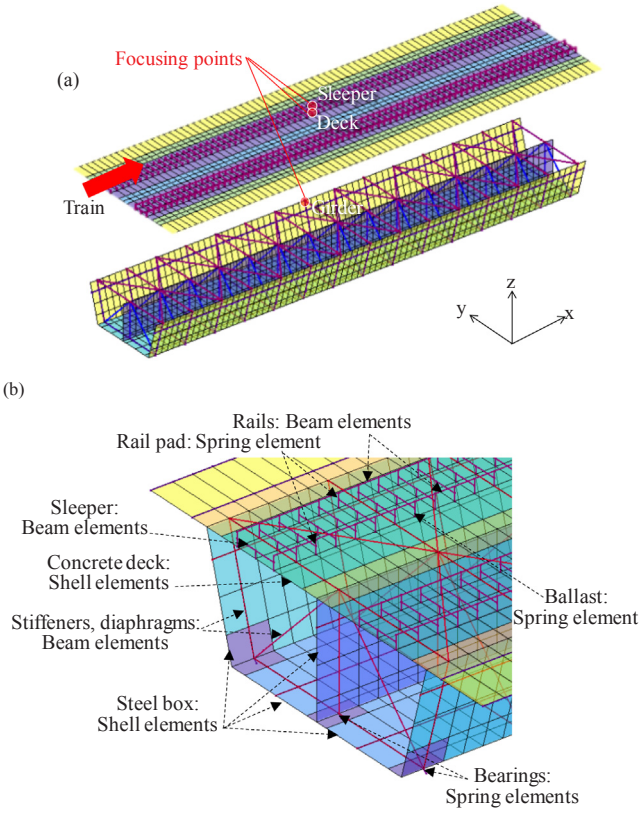

Fig. 4. Finite element model of the Sesia viaduct: (a) Global view of the model and focusing points, (b) Detailed view of the model.

Table 3
Material specifications of each element.

Member	Type	Stiffness K [MN/m]		
Pad	Spring	60.0/1pad		
Ballast	Spring	505/1sleeper	(vertical)	
	Spring	125/1sleeper	(longitudinal)	
	Spring	125/1sleeper	(horizontal)	
Member	Type	Elastic modulus E [kN/mm^2]	Moment of inertia I [m^4]	Mass M [kg/m]
Rail	Beam	206	3.2×10^{-5}	60.0
Sleeper	Beam	–	–	110
Stiffener	Beam	206	1.3×10^{-5}	18.2
Diaphragm			$-\ 9.0 \times 10^{-5}$	− 43.5
Ballast wall	Beam	30	1.1×10^{-3}	700
Safety barrier	Beam	30	1.1×10^{-2}	1610
Member	Type	Elastic modulus E [kN/mm^2]	Thickness t [m]	Density ρ [kg/m^3]
Deck	Shell	34.1	0.39–0.42	2500 (deck only) 4405 (with ballast)
Web	Shell	206	0.02	8010
Flange	Shell	206	0.02	8010

that the target structure is a linear time-invariant system [33,34]. The acceleration responses recorded over 5 s after train passage was selected and the modal characteristics were identified by the ERA method with 40 degrees of freedom.

2.3. Numerical computation

2.3.1. Structural model

Fig. 4 illustrates the finite element model of the Sesia viaduct. The concrete deck and steel box-girder are represented with shell elements, and the diaphragms, lateral stiffeners, diagonals, stiffeners at the bridge ends, sleepers and rails are modelled as beam elements. The ballast, rail pads and bridge bearing are modelled as spring elements. The other non-structural members, such as ballast walls and safety barriers, are not considered for the less effects as reported in [31]. The cross-sectional dimensions of each member were calculated, and the connections between the concrete deck and the steel girder upper flange were assumed to be rigid. As for the track members, the model was simplified as follows, based on past studies [35,36]. The sleepers are modelled as a rigid beam that reflects only the mass and the length, and the ballast mass was considered as a mass added to the concrete slab. The material properties of each element were set as shown in Table 3, based on the design specifications for the bridge. To express the rail deformation and local deck member vibration, the elements were divided into 1 m maximum in the x direction and 0.6 m maximum in the y direction. Following the design drawings, nodes corresponding to the bearings were set to determine constraints in the x and y directions. Both rail ends constrained the rotations of the z-axis and y-axis. However, the rigidity and mass of concrete and steel were corrected based on the identification results described later. The ballast stiffness in the vertical direction was calculated from the accelerations measured at the sleeper and at the deck just below the sleeper via a transfer function.

The modal damping ratios were set to 5% for vibration modes less than 10 Hz and 2% for modes of more than 10 Hz, in consideration of the modal identification results described below. The structural model included 3353 nodes and contained 4883 elements. The simulations were focused on the upper flange of the steel girder, the concrete deck and the sleeper at the mid-span. All focus points were located on side of the track over which the train passed. The modal-domain time-integration method considered 1000 modes of the structure's vibration, including the deformation of the track and rails in addition to the overall structural deformation. Several studies [24,37] also recommend that a frequency range up to 1.5 times the maximum frequency target should be considered when simulating modal domains. To verify the adequacy of this method, we also carried out numerical calculations that only considered modes up to the 100th order, which capture frequencies up to about 45 Hz (1.5 times more than 30 Hz).

To analyse the effect of train-structure interactions on the estimated maximum deck acceleration, we also carried out another numerical calculation with moving loads, in which the following vehicle in the vehicle-bridge system was modelled as a sequence of moving loads with the same axis weight and arrangement [13].

2.3.2. Vehicle model

Fig. 5 illustrates the numerical model of the vehicle and wheel/rail interaction. Each component of the car body, bogie and wheelset was modelled as a rigid body, and all of these were connected by springs and dampers. Each model vehicle has 31 degrees of freedom. The validity of the model was confirmed previously in full-scale experimental tests with real Shinkansen vehicles and rolling test beds in Japan [39]. To model the ETR 1000 train, eight model vehicles were connected, each being 24.9-m long, with the distance between bogies of 17.4 m and wheelset spacing of 2.85 m. The values of each spring, damper and mass were chosen from the literature [40] and separately performed measurements of the vehicle specifications. Dynamic interactive forces between wheels and rails are calculated on the basis of vertical and horizontal relative displacements between them. The nonlinear Hertz contact springs and creepage forces are considered in the normal and tangential directions of the contact surfaces as shown in Fig. 5.

2.3.3. Track irregularity

Although track irregularity effect on the vehicle-bridge interaction has been pointed out, track irregularities randomly generated from the

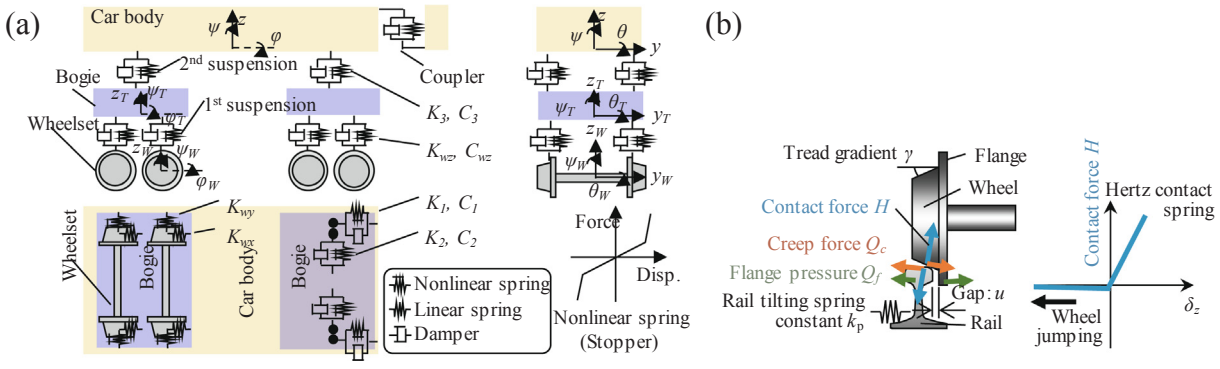

Fig. 5. Numerical model of (a) the ETR100 vehicle and (b) wheel/rail interaction.

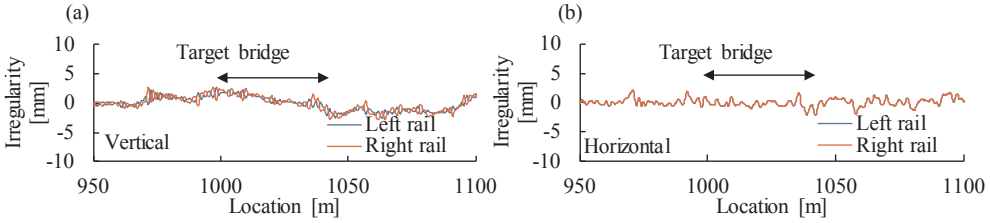

Fig. 6. Measured track irregularity: (a) vertical direction, and (b) horizontal direction.

spatial spectral density function are used for simulation in many literatures [10,29,38]. This research adopted irregularities actually measured to reproduce the bridge dynamics with high accuracy. Fig. 6 shows the rail irregularities employed in the numerical analysis. The irregularities in the dimensions of the rails on the vehicle running side were included, based on the vertical, horizontal and torsional components of the Sesia viaduct track displacement as measured by track-inspection vehicles. The measurement interval of track irregularity is 0.25 m. Therefore, the excitation frequency due to the track irregularity sufficiently covers up to 30 Hz under high-speed train running.

2.3.4. Train passage simulation

Numerical simulation of train passages using the numerical models of the Sesia viaduct and the ETR1000 train were conducted by DIASTARS III [39]. This simulation platform was developed by the railway technical research institute in Japan. In DIASTARS III, the dynamic interactions between wheels and rails is taken into account as shown in Fig. 5. For details about DIASTARS III, please refer to [39,41].

3. Experimental and numerical analysis results

3.1. Measured acceleration responses

Fig. 7 shows the 15 Hz LPF (black line) and 30 Hz LPF (grey line) acceleration data at each measurement point taken as the train passed over the bridge at 358 km/h. Acceleration data at other train speeds can be found in references [30,31]. The amplitude of 15 Hz LPF acceleration is significantly smaller than that of 30 Hz LPF acceleration.

Fig. 8 shows the acceleration spectra measured at different train speeds and at girder G2 and deck D2 measurement points while the train passed over the bridge. As the train speed increases, the peak frequencies shift to higher values. Moreover, the peak amplitude in the range 20–30 Hz is larger than that at around 4 Hz. The peak amplitude around 4 Hz is approximately the same for the deck and girder members, but in correspondence of the peak at 25 Hz, the deck point D2 vibrates with larger amplitude than that of girder G2. Therefore, the deck member vibration around 25 Hz is influenced by some contribution other than the global girder vibration.

3.2. Identification results

The vibration modes were identified based on the acceleration responses after train passage, and the global and local deck modes are shown in Figs. 9 and 10. It should be noted that the experimentally measured modal shapes are expressing the average values for all measured cases while the results shown in references [30,31] are representative values. The mode shapes were normalised to the maximum vibration amplitude. In addition, the vibration mode shapes are shown as calculated by the numerical model. In the global bending mode shown in Fig. 9, the girder and the deck vibrations have approximately the same mode amplitude. Additionally, in the global torsion mode, the centre of cross-section is a node, and both girders have opposite phase amplitudes. These global modes were distributed at frequencies under 20 Hz. On the other hand, in the local deck mode shown in Fig. 10, the mode amplitude of the deck vibration is equal to or larger than the amplitude of the girder vibrations. The frequencies of the local deck mode were distributed between 20 and 30 Hz.

Table 4 shows the averages of the natural frequencies and modal damping ratios along with their coefficients of variation (standard deviation/average value) [30,31]. The identified natural frequencies vary by approximately 3% at the maximum. The modal damping ratios vary more than the frequency, with variation coefficients from approximately 30% to a maximum of 130%. It should be noted that the modal damping ratio of the global modes are larger than those of the local deck modes.

Table 5 shows the natural frequencies of the Sesia viaduct that were identified in previous studies [23,24,42], and [43], along with our results. Our numerical calculations find a slightly higher natural

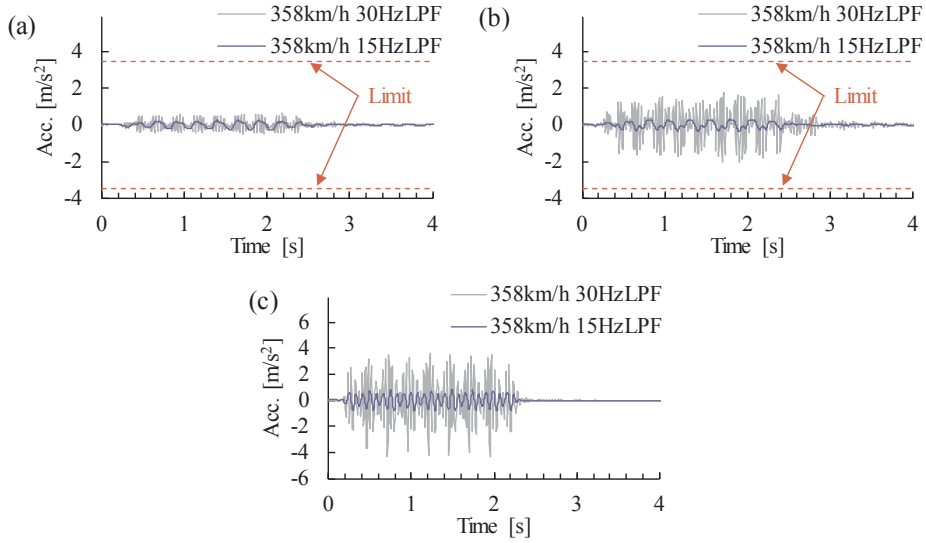

Fig. 7. 15 Hz LPF and 30 Hz LPF acceleration responses obtained during train passage at the speed of 358 km/h: (a) girder G2, (b) deck D2, and (c) sleeper S.

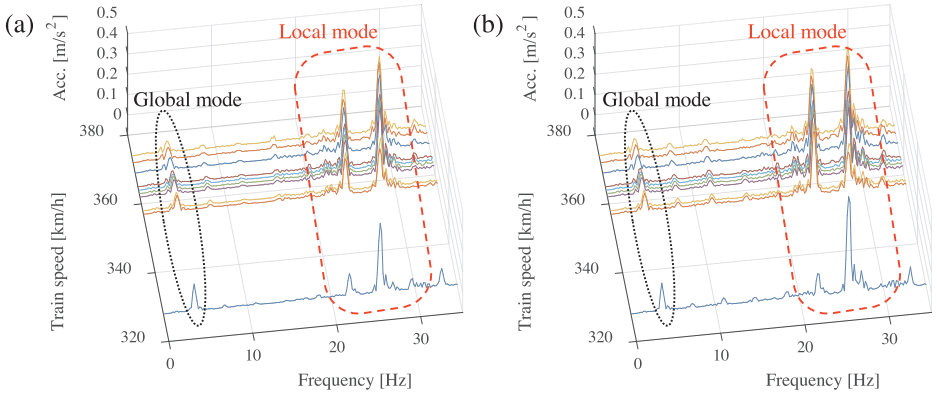

Fig. 8. Acceleration spectra during train passages at the speed of 328–374: (a) girder G2, (b) deck D2.

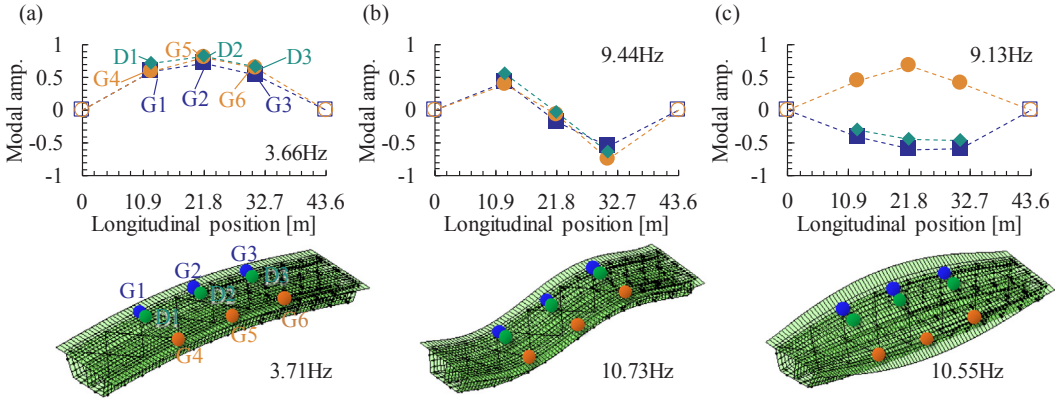

Fig. 9. Experimentally measured and numerically calculated global vibration modes: (a) first bending mode, (b) second bending mode, (c) first torsional mode.

frequency in the global modes. Considering this tendency and high damping ratio at low frequency mentioned above, it can be inferred that the interaction with subsoil can affect the identified result. However, numerical results agree with the identified ones within error of 5%. Moreover, the simulated natural frequencies of the local deck modes correspond precisely with our experimental results. Therefore, the numerical model is sufficiently accurate to reproduce the local vibration modes of bridge members to predict the deck acceleration.

The global modes up to about 20 Hz, except for the secondary torsional mode, generally agree with previously reported results. In the same table, the modes determined by considering interactions with adjacent bridges [23,24,29] are expressed in parentheses. These are vibration modes with the same mode shape and different natural frequencies that are caused by the interaction with adjacent bridges via the track and deck [24,29], but could not be identified from our local measurements of acceleration responses after train passage. The modes that are affected by interaction with the adjacent bridges are also included [23], which were identified from the measurements of the natural frequencies of Sesia viaduct based on the acceleration responses during train passages. Our discussion of the relationship between maximum acceleration and train speed that appears below concludes with empirical data that the vibration modes due to interactions with adjacent bridges are practically irrelevant as the train passes over the bridge. Therefore, we did not consider interactions with adjacent bridges.

3.3. Validation of acceleration responses

The acceleration responses during train passage were calculated from the numerical dynamic model. The numerical 15 Hz LPF and 30 Hz LPF acceleration responses were calculated via low-pass filter processing, just as the measured values were.

Fig. 11 plots the experimental and numerical 15 Hz LPF acceleration over time as the train passed over the bridge at 358 km/h. The 15 Hz LPF accelerations predicted by the numerical simulation in the girder, deck and sleeper coincide precisely with the actual measured values. This agreement confirms that the constructed numerical models can reproduce the global acceleration response accurately.

Fig. 12 plots the 30 Hz LPF acceleration at the train speed of 358 km/h. Even the simulated 30 Hz LPF values agree well with the experimental values.

Although the acceleration response of the sleepers is not typically included in the evaluations of maximum acceleration, the acceleration response of the sleepers near to the point of contact between the wheels and rails is an important indicator of the accuracy of numerical model. However, few previous studies have compared simulations of this acceleration with experimental measurements. As shown in Fig. 11 and Fig. 12, the responses and maxima values of the sleeper acceleration during train passage were accurately reproduced in our dynamic model.

3.4. Validation of acceleration spectra

Fig. 13 shows the log-scale acceleration spectra caused by trains passing at a speed of 358 km/h, in order to confirm the accuracy of the numerical calculations of accelerations in each frequency band. The spectra were calculated from the acceleration response during the 5 s of interest and included the time over which the train passed. The peak frequencies, peak amplitudes and peak shapes of the acceleration spectra as numerically calculated are in good agreement with the values measured at the girder, deck and sleeper. The notable difference between the numerical and experimental values in the frequency range under 5 Hz in the sleeper spectrum is inferred due to errors in the observations caused by the filter characteristics of the installed piezoelectric accelerometer.

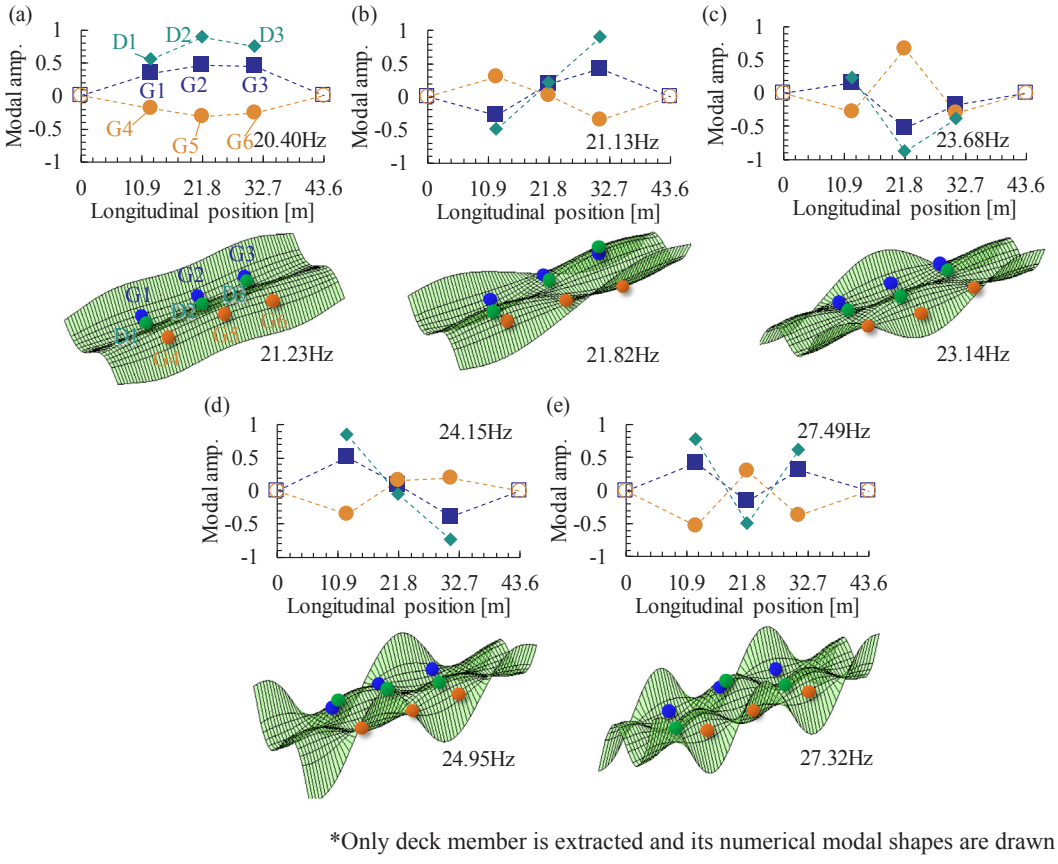

Fig. 10. Experimentally measured and numerically calculated local deck vibration modes: (a) first mode, (b) second mode, (c) third mode, (d) fourth mode, and (e) fifth mode. *Only deck member is extracted and its numerical modal shapes are drawn.

Table 4
Identified natural frequencies and modal damping ratios [30,31]

	Natural frequency [Hz]		Modal damping ratio	
Mode	Ave	Std./Ave	Ave	Std./Ave
First bending	3.66	0.019	0.046	0.640
Second bending	9.44	0.029	0.038	0.603
Third bending	17.82	0.023	0.036	0.385
First torsional	9.13	0.015	0.027	0.361
Second torsional	18.64	0.018	0.028	1.337
Third torsional	20.04	0.014	0.020	0.648
First local deck	20.40	0.004	0.013	0.370
Second local deck	21.13	0.004	0.015	0.320
Third local deck	23.68	0.011	0.011	0.415
Fourth local deck	24.15	0.002	0.011	0.394
Fifth local deck	27.49	0.007	0.015	0.597

Fig. 14 shows the linear-scale acceleration spectra measured at the train speed of 358 km/h, which confirms the accuracy of our calculations of the peak amplitude of the acceleration response. Peaks appear at approximately 4 Hz and around 20–30 Hz in the spectra at the girder (G2) and deck (D2), and at all frequencies the amplitudes are in good agreement. Therefore, the numerical model constructed in this study can accurately evaluate the degree to which each dominant structural vibration component contributes to the bridge's acceleration response.

It should be noted that verifications at other train speeds also show results similar to the ones reported in Figs. 11-14. The interested reader is referred to the past literature [31].

3.5. Validation of maximum acceleration

Fig. 15 shows the comparison between the numerical and the experimental maximum values of 15 Hz LPF and 30 Hz LPF accelerations at each train speed. In the 15 Hz LPF acceleration data shown in Fig. 15(a), the numerical maximum values for the girder (G2) and the deck (D2) are in good agreement with the experimental values. As for the sleeper (S), though the variation is somewhat larger than the girder

Table 5
Comparison of the natural frequencies with the existing researches.

	Natural frequency [Hz]				
	Present	Ref. [23,24,42]	Ref. [42]	Ref. [31]	Present
				FE Model	FE model
Method	ERA	SSI [43]	Poly-MAX [44]		
Mode	Free vib	Free vib	Ambient		
First bending	3.66	3.90 (4.14)	3.63 (4.13)	3.71	3.71
Second bending	9.44	10.00 (10.41)	9.93 (10.57)	10.74	10.73
Third bending	17.82	–	17.40	19.89	19.87
First torsional	9.13	9.00 (9.13)	8.37 (8.94)	10.56	10.56
Second torsional	18.64	–	11.26 (14.36)	18.44	18.40
Third torsional	20.04	–	19.20	20.03	20.01
First local deck	20.40	–	–	21.23	21.23
Second local deck	21.13	–	–	21.84	21.82
Third local deck	23.68	–	–	23.15	23.14
Fourth local deck	24.15	–	–	24.99	24.95
Fifth local deck	27.49	–	–	27.36	27.32

*() expresses the frequency considering the effects of interaction with the adjacent bridges.

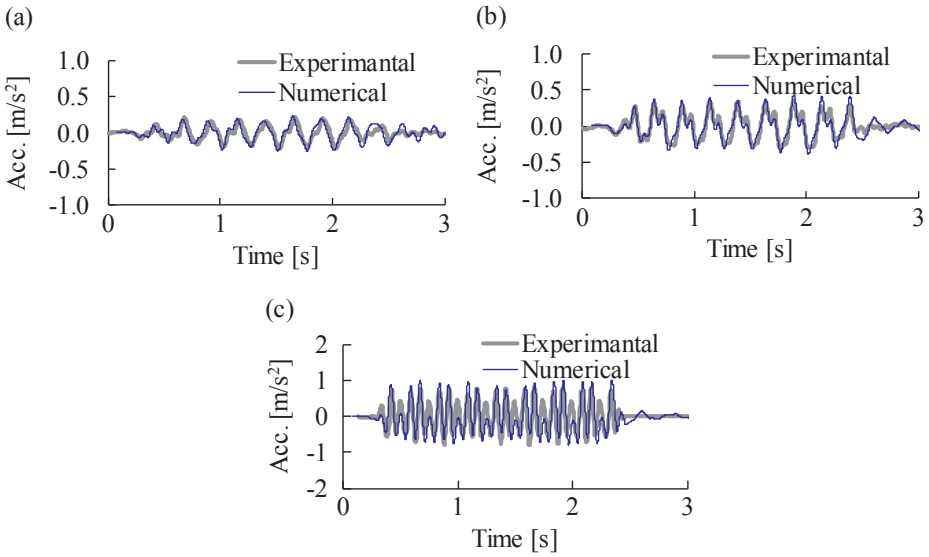

Fig. 11. Experimental and numerical comparison for 15 Hz LPF acceleration responses at the train speed of 358 km/h at (a) girder G2, (b) deck D2, and (c) sleeper S.

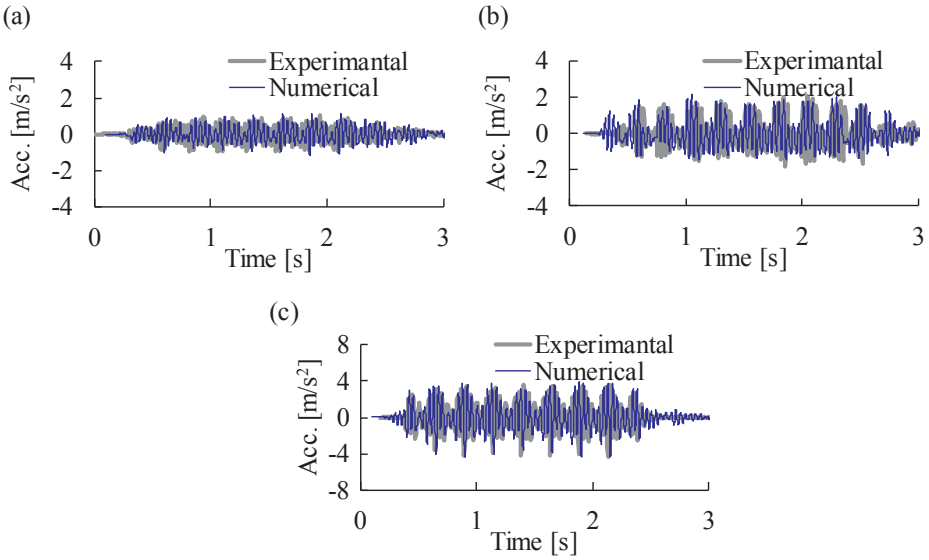

Fig. 12. Experimental and numerical comparison for 30 Hz LPF acceleration responses at the train speed of 358 km/h at (a) girder G2, (b) deck D2, and (c) sleeper S.

and deck, the numerical results show the same trend as the experimental values.

The global bending mode resonates at a train speed of approximately 330 km/h, as indicated by the peak in Fig. 15 (a). The model of the Sesia viaduct constructed in this study does not consider the influence of interaction with adjacent bridges, but the maximum value of the 15 Hz LPF acceleration coincides with the measured values precisely. In addition, if the other first-order mode in which interaction with adjacent bridges is considered exists and resonates when the train passes, a peak corresponding to the resonance should appear in the measured values in Fig. 15(a). However, only the peak corresponding to the first-order mode that does not consider the interaction with adjacent bridges appears in Fig. 15(a). Therefore, as described above, the influence of the interaction with adjacent bridges is negligible when evaluating the acceleration during train passage, especially when resonance occurs.

Fig. 15(b) shows the maximum value of the 30 Hz LPF acceleration. These numerical results also coincide well with the experimental values for the girder (G2), deck (D2) and the sleeper (S). The peaks of the 30 Hz LPF maximum acceleration appear near 290, 315, 370 km/h, as shown in Fig. 15(b). Therefore, when we modelled and calibrated our measurements to include higher-order modes of the deck member vibration, the maximum value of the deck acceleration up to 30 Hz as specified by Eurocode [4] is evaluated accurately in our numerical calculations. In addition, the maximum acceleration of the Sesia Bridge did not exceed the reference value of 3.5 m/s^2 for the girder and deck, even when simulated up to a maximum train speed of 400 km/h.

4. Discussion of high-order resonance

4.1. High-order excitation frequency of passing train

In the accelerations of the deck (D2) shown in Fig. 15(b), peaks appear at several train running speeds. Since these peaks do not appear in Fig. 15(a), the peaks shown in Fig. 15(b) must be caused by resonance between the local deck modes at the frequency of 15–30 Hz and the high-order excitation created by the travelling train. To investigate this high-order excitation component, the spectra of moving concentrating excitation forces were calculated based on the axle arrangement of the ETR 1000, illustrated in Fig. 16, and using a method

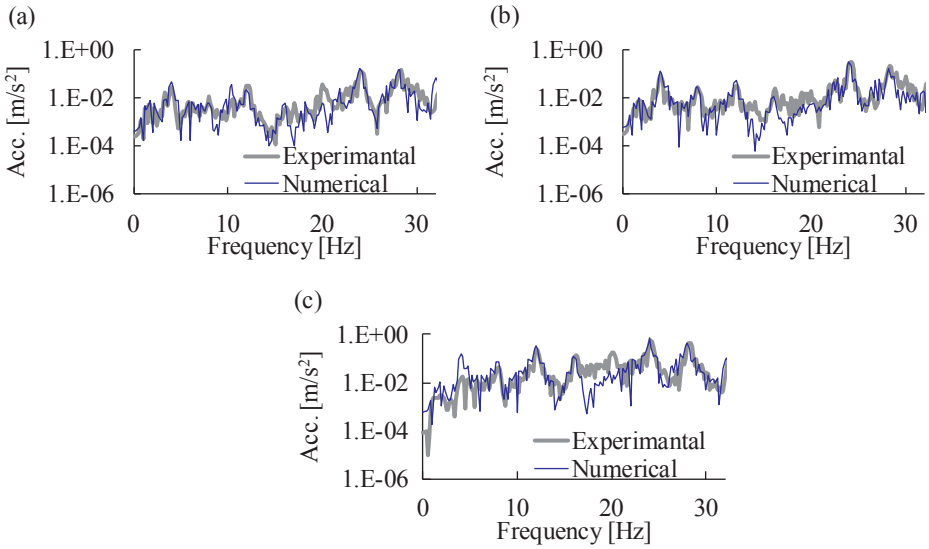

Fig. 13. Experimental and numerical comparison for log-scaled acceleration spectra at the train speed of 358 km/h at (a) girder G2, (b) deck D2, and (c) sleeper S.

published previously [45,46]. If the train load is assumed to be a concentrated load sequence of magnitude 1 at each axis, the Fourier transform of the train load [31,45] is calculated with equation (1).

$$|H_c(\omega)| = |H_a(\omega)| \times |H_b(\omega)| \times |H_{L_c}(\omega)| \tag{1}$$

$$|H_a(\omega)| = 2\,|\cos(a\omega/2V)| \tag{2}$$

$$|H_b(\omega)| = 2\,|\cos(b\omega/2V)| \tag{3}$$

$$|H_{L_c}(\omega)| = 2\left|\frac{\sin(n_c L_c \omega/2V)}{\sin(L_c\omega/2V)}\right| \tag{4}$$

Here, ω is the angular frequency, V is the train speed [m/s], a is the axle interval [m], b is the bogie-centre interval [m], and L_c is the vehicle length [m].

Fig. 17(a) shows each spectrum of the excitation force of the ETR 1000 when travelling at 330 km/h. The excitation force spectrum is multiplied by the spectra of the vehicle interval, the bogie-centre interval and the axle interval.

The i-th order resonance train speed V_i can be calculated from the vehicle interval L_c and j the vibration mode natural frequency f_j [47–49].

$$V_i = \frac{L_c f_j}{i} \tag{5}$$

Given the dimensions of the ETR 1000 train, the sixth- and seventh-order resonance peaks are prominent in addition to the first-order resonance. Fig. 17(b) shows the spectrum of excitation force of the ETR 1000 at speeds 200–400 km/h. As the train running speed increases, each frequency peak shifts to a higher value. For train speeds up to 400 km/h, the first, third, sixth and seventh peaks caused by the vehicle length are the dominant exciting forces at frequencies under 30 Hz. Focusing on the vibrations from 15 to 30 Hz, which generated large accelerations in our measurements, the sixth- and seventh-order excitation frequencies of the car length are the dominant contributions.

4.2. High-order resonance and prominent local deck vibration modes

The peaks near 290, 315, 370 km/h on the 30 Hz LPF maximum acceleration and corresponding vibration modes are discussed below.

Table 6 and Fig. 18 show the resonance speed bands of each

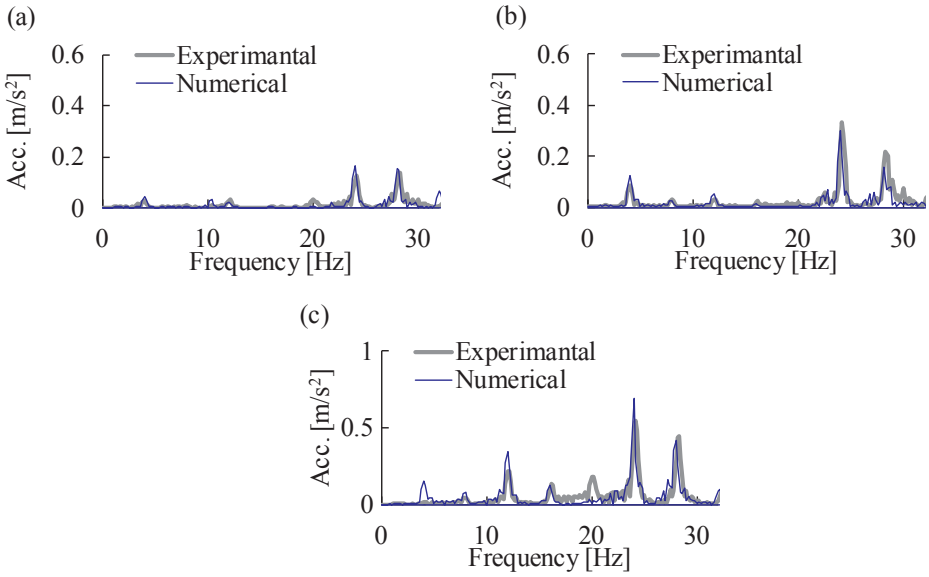

Fig. 14. Experimental and numerical comparison for linear-scaled acceleration spectra at the train speed of 358 km/h at (a) girder G2, (b) deck D2, and (c) sleeper S.

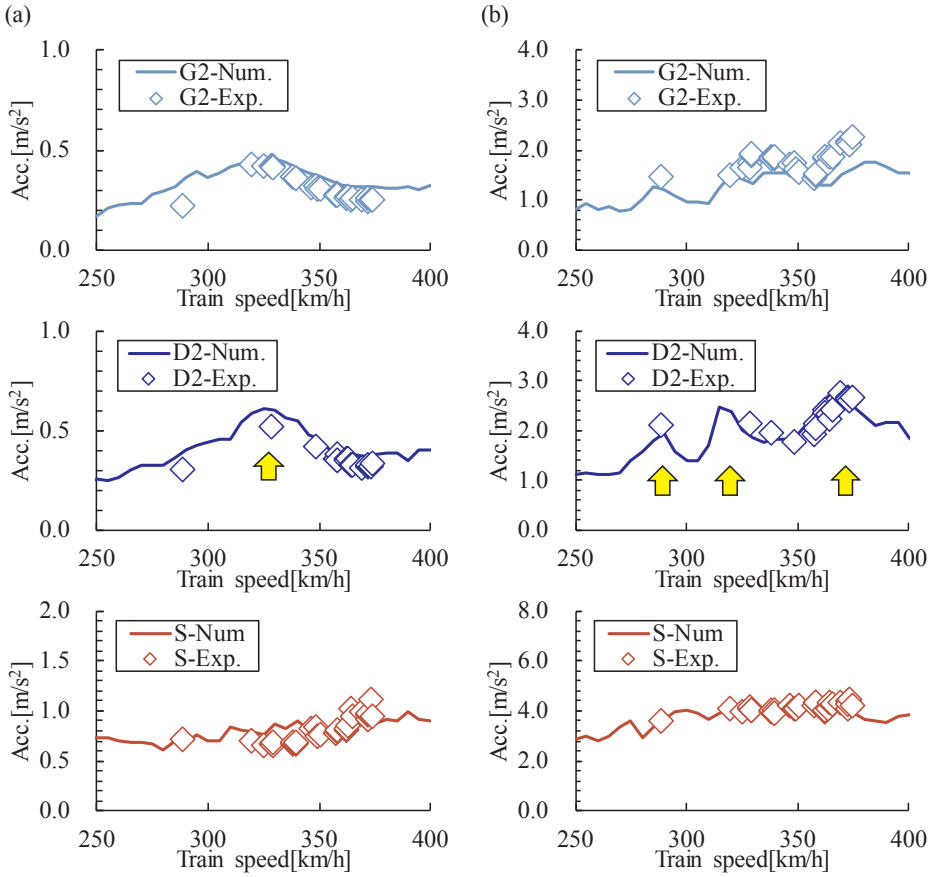

Fig. 15. Experimental and numerical comparison for maximum acceleration of (a) 15 Hz LPF and (b) 30 Hz LPF.

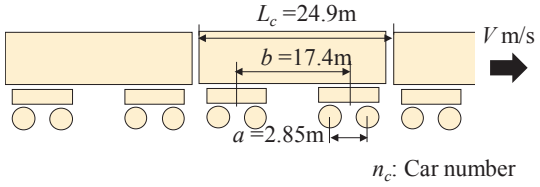

Fig. 16. Axle and bogie intervals and vehicle length of ETR1000.

vibration mode as calculated by Eq. (5). Sixth and seventh resonance speeds (i.e. i = 6and7 in Eq. (5)) in which the dominant exciting forces exist are focused. The figure also shows the predicted maximum values of the 15 Hz LPF and the 30 Hz LPF acceleration at each travelling speed, as calculated in our dynamic calculations. The resonance speed band of each vibration mode is expressed as a range around the average value ± 2σ (standard deviation), as determined from the experimental results. Table 6 and Fig. 18 (a) and (b) show the sixth and seventh resonance speed bands (i.e. i = 6and7 in Eq. (5)) for each vibration mode.

As shown in Fig. 18(a) and (b), the sixth resonance (i = 6) of the second-order local deck mode and the seventh-order resonance (i = 7) of the fourth local deck mode are generated at train speeds of around 315 km/h, at which a peak appears at the maximum value of the 30 Hz LPF acceleration. In addition, the sixth resonance speed of the third- and fourth-order local deck modes are close to the resonance peak in the 30 Hz LPF acceleration at the train speed of 370 km/h. Therefore, we conclude that the sixth and seventh resonances of these higher-order local deck modes make a significant contribution to the maximum acceleration at 30 Hz.

4.3. Effect of track deformation

In general, modal reduction is performed to improve the efficiency of numerical computations of such a large-scale dynamical model of the bridge-vehicle system. In the present case, however, we included the numerical modes of the structure up to 1.5 times of the 30 Hz evaluation frequency, i.e. 45 Hz, as suggested by others in the literature [23,24] and [37]. On the other hand, when evaluating the local resonance behaviour of the deck members, the response of the tracks sitting on top of the members may also be important. To understand the effect of the track's resonance, we compared computations of the following three situations:

- Case G includes only the global modes, with four bending and four torsional modes.
- Case G-L includes eight global modes and 10 local deck modes. The maximum frequency of 46 Hz is approximately equal to 1.5 times the standard frequency.
- Case G-L-T includes the modes of Case G-L plus 20 track deformation modes, which vibrate at frequencies of 100 to 150 Hz, as shown in Fig. 19.

Fig. 20 shows the numerically calculated maximum 30 Hz LPF accelerations at the girder, deck and sleeper. The maximum accelerations in Case G are much lower than in the other cases. In addition, some peaks shown in Case G-L and Case G-L-T do not appear in Case G, since Case G does not consider the local deck modes or the track deformation modes. Comparing the Cases G-L and G-L-T at the girder G2 and deck D2, the maximum acceleration predicted in Case G-L-T is twice the size of the maximum acceleration calculated more simply. The difference is particularly pronounced in the high-speed region, over 320 km/h. This

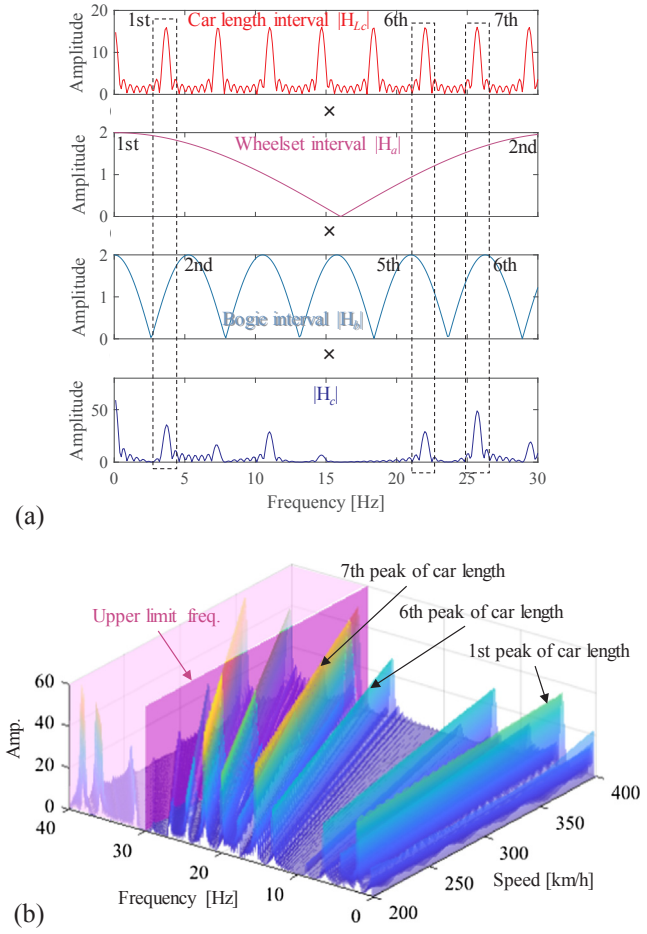

Fig. 17. Spectra of excitation force of ETR 1000: (a) components of excitation spectrum at 330 km/h, (b) relationship with train speed.

Table 6
List of sixth and seventh-order resonance speeds (i = 6, 7).

Mode	Resonance speeds [km/h]	
	i = 6 (-2σ, $+2\sigma$)	i = 7 (-2σ, $+2\sigma$)
First bending	(52.4, 56.5)	(44.9, 48.5)
Second bending	(132.3, 148.6)	(113.4, 127.4)
Third bending	(253.0, 277.4)	(216.8, 237.7)
First torsional	(131.8, 139.9)	(113.0, 119.9)
Second torsional	(267.4, 287.3)	(229.2, 246.3)
Third torsional	(289.8, 306.5)	(248.4, 262.8)
First local deck	(297.5, 309.6)	(255.0, 265.4)
Second local deck	(309.4, 319.4)	(265.2, 273.8)
Third local deck	(344.6, 360.1)	(295.4, 308.7)
Fourth local deck	(352.9, 365.8)	(302.5, 313.6)
Fifth local deck	(403.3, 414.8)	(345.7, 355.5)

difference is explained by the track deformation modes. Thus, we conclude that track deformations amplify the excitation force from the travelling vehicle, thereby increasing the maximum acceleration of the structure when trains are passing at very high speeds. The maximum acceleration of the sleeper near the excitation point is plotted in Fig. 20(c). The maximum sleeper acceleration in Case G and G-L is less than 1/4 of that in Case G-L-T. This result supports our inference that the track deformation amplifies the effect of the excitation force. Thus, if engineers are evaluating the maximum acceleration with numerical simulations, the track deformation modes and the local deck member modes should be considered along with the conventional global

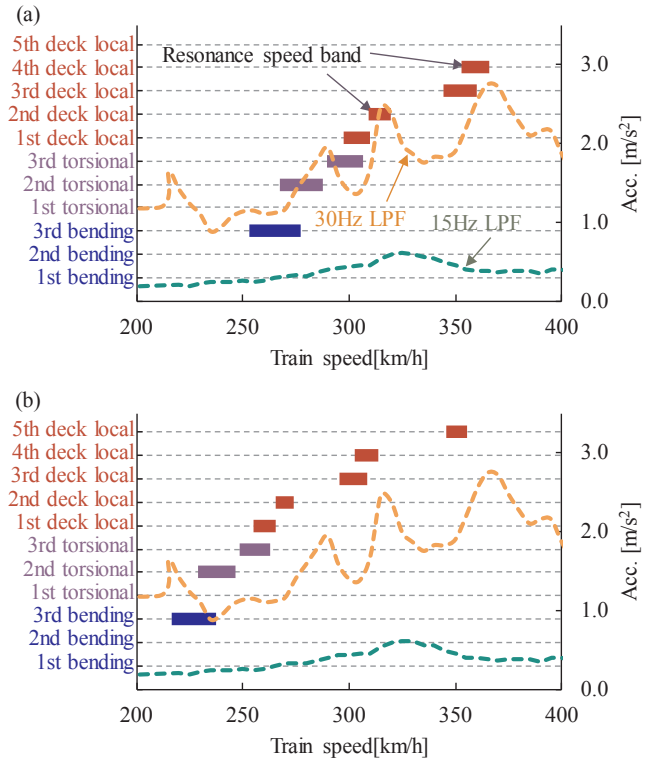

Fig. 18. Maximum acceleration and resonance speed bands of the structural vibration modes for (a) sixth resonance and (b) seventh resonance with vehicle length of 24.9 m. The resonance speed bands are shown as the measured average value ± 2σ.

vibration modes.

4.4. Effect of the vehicle-bridge interaction

Fig. 21 shows the maximum acceleration in the case that the travelling vehicle was modelled as a sequence of moving loads with the same axial load and same axle arrangement, referred to as the moving loads model. Generally, the global bridge responses of the girder as calculated by the vehicle-bridge interaction model are smaller than they are when calculated by the moving loads model due to the propagation and transfer of bridge vibration energy to the travelling vehicle via dynamic interactions between the bridge and passing vehicle (additional damping) [3,13,46]. The maximum 15 Hz LPF acceleration is shown in Fig. 21(a), in which the first global bending mode is a dominant component. This data also shows the widely-known tendency that the results of the moving load model will be larger than those of the vehicle-bridge interaction model because this model better accounts for resonance. However, the maximum 30 Hz LPF deck acceleration computed from the moving load model as shown in Fig. 21(b) is rather lower than that computed with the vehicle-bridge interaction model for high speeds over 250 km/h. From this result, we infer that the influence of vehicle-bridge interaction, representing the transfer of energy between the vehicle and the structure, is different on the global modes vibrating at under 15 Hz and the local deck modes over 15 Hz. In other words, the additional damping effect that the moving loads model captures is dominant only for the global mode at low frequencies. For the local deck modes over 15 Hz, on the other hand, the dynamic amplification effect due to the axle load variation is dominant. One of the dominant axle load variations is caused by the interaction between the wheelset and rails as the wheelset moves on the deformed rails, as discussed in Section 4.3. These results indicate that both the vehicle-bridge interaction and the track (rails) deformation modes are important when predicting the maximum 30-Hz acceleration with

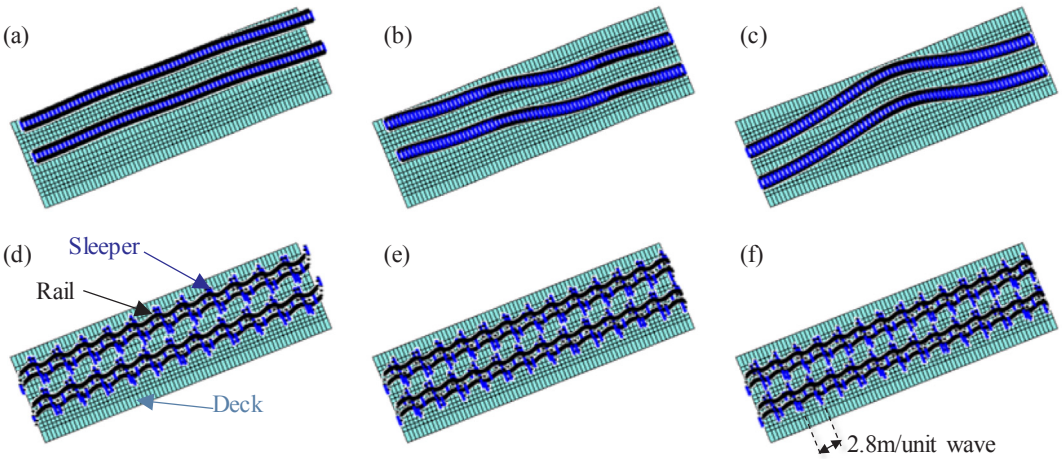

Fig. 19. Examples of track deformation modes; (a) translation track mode (93 Hz), (b) rotation track mode (94 Hz), (c) 1rd order track mode (96 Hz), (d) 12th order track mode (131 Hz), (e) 13th order track mode (132 Hz), and (f) 14th order track mode (133 Hz).

numerical simulations.

4.5. Method for determining the appropriate modes for bridge-safety evaluations

Fig. 22 illustrates the concept of how the exciting force is affected by the wheelsets running on deformed, rather than rigid, rails. If we consider the mode with which the rail deforms at a constant wavelength L_M, the excitation frequency of the axle running at speed V is V/L_M [Hz]. To consider excitation forces that vary at frequencies up to 30 Hz, the following equation should be satisfied for the wavelength L_M at the maximum mode order M [31].

$$V/L_M > 30 \tag{6}$$

Thus, the wavelength of the rail deformation L_M can be expressed as follows.

$$L_M < V/30 \tag{7}$$

Assuming the speed range that needs to be accounted for is 300–400 km/h, the calculations will need to consider modes of lesser order than the rail deformation mode with wavelength $L_M < 300/3.6/30 \approx 2.8$[m]. Because the natural frequency of the vibration mode satisfying equation (7) will generally greatly exceed 30 Hz, the prediction may underestimate the excitation force if the prediction only considers 1.5 times the standard limit of 30 Hz.

Fig. 19 also shows rail deformation with wavelength of 2.8 m at 133 Hz, which is the 14th-order track vibration mode. This is a wavelength with the above-mentioned limit of 2.8 m. Therefore, by considering modes of up to about the 20th order we conclude that the track vibrations can be reproduced with very high accuracy.

Fig. 23 shows the maximum deck acceleration estimated by numerical calculations that include various orders of track deformation modes up to 50th, 20th, 5th, and 0th order. The 50th order and 20th order satisfy the condition of Eq. (7), while the 5th order includes the only 5 modes with vibrations of up to approximately 100 Hz. The case that did not consider any track vibration included only structural vibrations up to 45 Hz.

Fig. 23 points out that when considering only a few track deformation modes, the evaluation will underestimate the maximum acceleration of the deck. On the other hand, the results when considering

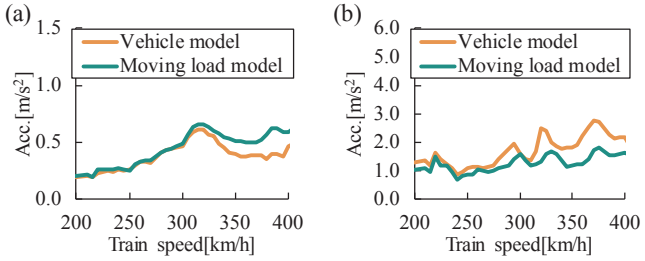

Fig. 21. Influence of vehicle-bridge interaction on the maximum deck acceleration with the 15 Hz LPF (a) and the 30 Hz LPF (b).

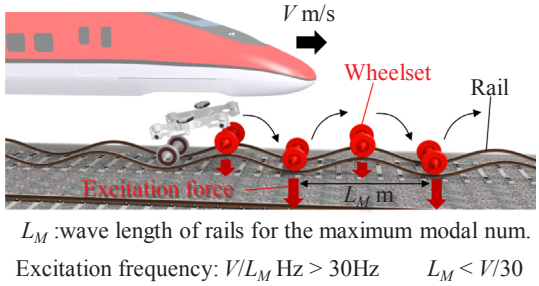

Fig. 22. Conceptual illustration of excitation force of travelling vehicle and rail deformation modes.

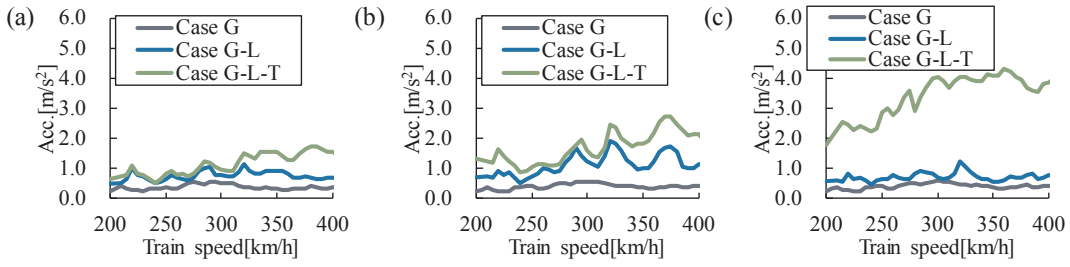

Fig. 20. Influence of including structural modes in numerical calculations of the 30 Hz LPF maximum acceleration at (a) girder G2, (b) deck D2, and (c) sleeper S.

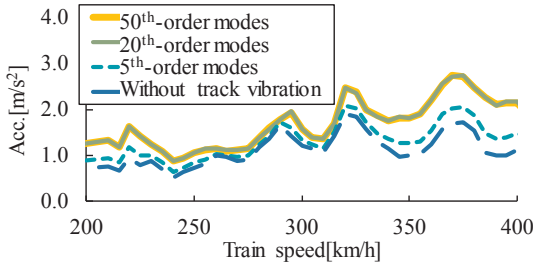

Fig. 23. Influence of the inclusion of the track deformation modes on the maximum deck acceleration.

up to the 20th-order track modes, satisfying the condition of Eq. (7), returns almost the same results as the simulation that considers up to the 50th-order track modes. Therefore, we conclude that simulations should consider track vibrations including modes up to the 20th order in order to give accurate and efficient estimations of the maximum deck vibration under the Eurocode standards.

5. Conclusion

To investigate how the maximum deck acceleration is typically evaluated for structures making up the European high-speed railway, this study presented in-situ measurements and numerical calculations that included the influence of local deck vibrations on the movement of a specific steel-concrete composite railway bridge. We draw the following five main conclusions from our results.

(1) Based on tests with trains passing across the bridge up to the speed of 374 km/h, both global and local deck vibrational modes were detected at frequencies up to 30 Hz. This empirical data revealed that the high-order resonances of several local vibrational modes with natural frequencies of 20–30 Hz have a dramatic influence on the maximum deck acceleration.
(2) The acceleration responses, spectra and maximum value during train passage as calculated in numerical simulations of the vehicle-bridge system are in good agreement with the values measured at the girder, deck, and sleeper.
(3) Experimental and numerical analysis of the identified modes and the maximum accelerations of the deck revealed that the high-order (sixth and seventh) resonances between the high-order (third, fourth and fifth) local deck modes and the excitation force of the train contribute to the dominant component in the maximum deck acceleration at frequencies of up to 30 Hz.
(4) Comparison of numerical calculations that include or exclude the local deck modes, track deformation modes and the vehicle-bridge interaction showed that high accuracy estimations of the maximum deck acceleration require modelling of the local modes, track deformation modes and vehicle-bridge interaction, along with the conventionally considered global vibrational modes. The absence of any of these components could lead to an underestimation of the maximum acceleration, since the travelling vehicle excites the bridge deck as the wheelset passes on the deformed rails.
(5) Using these results, we proposed a method for determining the order of the maximum track deformation modes. The ranking is based on the relationship between the wavelength of any rail deformation and the vibration period caused by a travelling train. Moreover, by considering track deformation modes of up to the 20th order, we found that the effect of the periodic train loads is amplified by the vibration of the rails.

Several issues remain for future research. First, although the target bridge is standard for Italy's high-speed railway, our findings are limited to this bridge. Data will need to be collected from bridges of various lengths and structures. Secondly, a more simple and generalisable numerical model should be developed, because detailed structural models and computations of vehicle-bridge interaction will be time- and cost-intensive, in practice. Finally, we only considered how to evaluate bridges against the maximum acceleration criteria of 3.5 m/s^2 at 30 Hz specified in Eurocode standards. However, much uncertainty remains about the influence of high-order resonances at scale of deck members level on ballast stability. For example, if the ballast stability is influenced by the duration of vibration, the ballast might not become unstable when vibrating in the sixth or seventh resonant mode. Thus, more calculations will be needed to clarify the influence of the upper limit frequency and duration on the bridge's tendency to prevent maximum acceleration exceeding 3.5 m/s^2.

Acknowledgements

This study was conducted as a part of an international collaboration between Politecnico di Milano, Department of Mechanical Engineering in Italy and the Railway Technical Research Institute in Japan.

Appendix A. Supplementary material

Supplementary data to this article can be found online at https://doi.org/10.1016/j.engstruct.2019.109736.

References

[1] Design RS. Design standards for railway structures and commentary (concrete structures). Tokyo: Railway Technical Research Institute; 2007.
[2] Xia H, Zhang N. Dynamic analysis of railway bridge under high-speed trains. Comput Struct 2005;83(23–24):1891–901.
[3] ERRI D214 Committee. Rail bridges for speeds higher than 200 km/h. Research Report of the European Rail Research Institute; 1999.
[4] CEN E. 1: Actions on structures-Part 2: Traffic loads on bridges. EN 1991: 2, 6, 2003.
[5] Cantero D, Karoumi R. Numerical evaluation of the mid-span assumption in the calculation of total load effects in railway bridges. Eng Struct 2016;107:1–8.
[6] Brozzetti J. Design development of steel-concrete composite bridges in France. J Constr Steel Res 2000;55(1–3):229–43.
[7] Bucknall I, New Eurocode requirements for the design of high speed railway bridges. In IABSE Symposium Report. International Association for Bridge and Structural Engineering, vol. 87, No. 12; 2003, January. pp. 17-24.
[8] Ribeiro D, Calçada R, Delgado R, Brehm M, Zabel V. Finite element model updating of a bowstring-arch railway bridge based on experimental modal parameters. Eng Struct 2012;40:413–35.
[9] Goicolea JM, Dominguez J, Navarro JA, Gabaldon F. New dynamic analysis methods for railway bridges in codes IAPF and Eurocode 1. Railway Bridges Design, Construction and Maintenance, Madrid 2002. p. 1–43.
[10] Arvidsson T, Karoumi R, Pacoste C. Statistical screening of modelling alternatives in train–bridge interaction systems. Eng Struct 2014;59:693–701.
[11] Martínez-Rodrigo MD, Lavado J, Museros P. Dynamic performance of existing high-speed railway bridges under resonant conditions retrofitted with fluid viscous dampers. Eng Struct 2010;32(3):808–28.
[12] Lavado J, Doménec A, Martínez-Rodrigo MD. Dynamic performance of existing high-speed railway bridges under resonant conditions following a retrofit with fluid viscous dampers supported on clamped auxiliary beams. Eng Struct 2014;59:355–74.
[13] Liu K, De Roeck G, Lombaert G. The effect of dynamic train–bridge interaction on the bridge response during a train passage. J Sound Vib 2009;325(1–2):240–51.
[14] Kang C, Schneider S, Wenner M, Marx S. Development of design and construction of high-speed railway bridges in Germany. Eng Struct 2018;163:184–96.
[15] Schneider S, Marx S. Design of railway bridges for dynamic loads due to high-speed traffic. Eng Struct 2018;174:396–406.
[16] Matsuoka K, Kaito K, Watanabe T, Sogabe M. Identification of high-order local vibration properties of RC viaduct. in dynamics of bridges. New York, NY: Springer; 2011. p. 171–8.
[17] Zhang X, Li X, Hao H, Wang D, Li Y. A case study of interior low-frequency noise from box-shaped bridge girders induced by running trains: its mechanism, prediction and countermeasures. J Sound Vib 2016;367:129–44.
[18] Watanabe T, Matsuoka K, Tokunaga M, Sogabe M. Vibration Reduction Countermeasures of Railway Concrete Viaduct. In MATEC Web of Conferences. EDP Sciences, Vol. 24. 2015. p. 08003.
[19] Martínez-Rodrigo MD, Lavado J, Museros P. Transverse vibrations in existing railway bridges under resonant conditions: Single-track versus double-track configurations. Eng Struct 2010;32(7):1861–75.
[20] Malveiro J, Ribeiro D, Calçada R, Delgado R. Updating and validation of the dynamic model of a railway viaduct with precast deck. Struct Infrastruct Eng 2014;10(11):1484–509.

[21] Malveiro J, Ribeiro D, Sousa C, Calçada R. Model updating of a dynamic model of a composite steel-concrete railway viaduct based on experimental tests. Eng Struct 2018;164:40–52.
[22] Bebiano R, Calçada R, Camotim D, Silvestre N. Dynamic analysis of high-speed railway bridge decks using generalised beam theory. Thin-Walled Struct. 2017;114:22–31.
[23] Liu K, Reynders E, De Roeck G, Lombaert G. Experimental and numerical analysis of a composite bridge for high-speed trains. J Sound Vib 2009;320(1–2):201–20.
[24] Liu K, Lombaert G, De Roeck G. Dynamic analysis of multispan viaducts with weak coupling between adjacent spans. J Bridge Eng 2013;19(1):83–90.
[25] Chellini G, Nardini L, Salvatore W. Dynamical identification and modelling of steel–concrete composite high-speed railway bridges. Struct Infrastruct Eng 2011;7(11):823–41.
[26] Zhou H, Liu K, Shi G, Wang YQ, Shi YJ, De Roeck G. Fatigue assessment of a composite railway bridge for high speed trains. Part I: Modelling and fatigue critical details. J Constr Steel Res 2013;82:234–45.
[27] Liu K, Zhou H, Shi G, Wang YQ, Shi YJ, De Roeck G. Fatigue assessment of a composite railway bridge for high speed trains. Part II: conditions for which a dynamic analysis is needed. J Constr Steel Res 2013;82:246–54.
[28] Chellini G, Nardini L, Salvatore W, Sorrentino G, Tisalvi M. Global and local dynamic behaviour of the Sesia viaduct, a steel-concrete composite railway bridge on the HS line Turin-Milan. In IOMAC 2009 International Operational Modal Analysis Conference, Vol. 2, 2009. pp. 603–611.
[29] Guo WW, Xia H, De Roeck G, Liu K. Integral model for train-track-bridge interaction on the Sesia viaduct: Dynamic simulation and critical assessment. Comput Struct 2012;112:205–16.
[30] Somaschini C, Matsuoka K, Collina A. Experimental analysis of a composite bridge under high-speed train passages. Procedia Eng 2017;199:3071–6.
[31] Matsuoka K., Collina A., Sogabe M., Watanabe T. High-Order Resonance of Deck Member of Composite Bridge and Acceleration Evaluation in European High-Speed Railway. Journal of Japan Society of Civil Engineers, Ser. A1 (Structural Engineering & Earthquake Engineering (SE/EE)), 74, 2018. P. 125–144. (In Japanese).
[32] Cantero D, Ülker-Kaustell M, Karoumi R. Time–frequency analysis of railway bridge response in forced vibration. Mech Syst Sig Process 2016;76:518–30.
[33] Juang JN, Pappa RS. An eigensystem realization algorithm for modal parameter identification and model reduction. J. Guidance Control Dynam. 1985;8(5):620–7.
[34] Matsuoka K., Kaito K., Watanabe T., Sogabe M. Identification of Dynamic Properties of Open-Deck Viaducts Under Passing Train Loads. In Civil Engineering Topics, Vol. 4. New York, NY: Springer; 2011. pp. 155-162.
[35] Aikawa A, Urakawa F, Abe K, Namura A. Dynamic characteristics of railway concrete sleepers using impact excitation techniques and model analysis. In 9th World Congress on Railway Research (WCRR), French Railways (SNCF). Paris: Publication Service; 2011.
[36] Knothe KL, Grassie SL. Modelling of railway track and vehicle/track interaction at high frequencies. Veh Syst Dyn 1993;22(3–4):209–62.
[37] Tournour MA, Atalla N, Chiello O, Sgard F. Validation, performance, convergence and application of free interface component mode synthesis. Comput Struct 2001;79(20–21):1861–76.
[38] Salcher P, Adam C. Modeling of dynamic train–bridge interaction in high-speed railways. Acta Mech 2015;226(8):2473–95.
[39] Tanabe M, Wakui H, Matsumoto N, Okuda H, Sogabe M, Komiya S. Computational model of a Shinkansen train running on the railway structure and the industrial applications. J Mater Process Technol 2003;140(1–3):705–10.
[40] Bionda S., Bocciolini L., Bon A., Braghin F., Brughera F., Cazzulani G., Prone L. Dynamic homologation tests of ETR1000-V300Zefiro up to 350km/h. In 11th World Congress on Railway Research (WCRR 2016). 2016. pp. 1–8.
[41] Tanabe M, Matsumoto N, Wakui H, Sogabe M, Okuda H, Tanabe Y. A simple and efficient numerical method for dynamic interaction analysis of a high-speed train and railway structure during an earthquake. J Comput Nonlinear Dyn 2008;3(4):041002.
[42] Liu K., Reynders E., De Roeck G. Experimental validation of the dynamic interaction analysis between high-speed trains and the Sesia viaduct. IMAC26, Orlando. 2008.
[43] Chellini G, Nardini L, Liu K, Reynders E, Peeters B, De Roeck G, et al. February). Experimental dynamic analysis of the Sesia Viaduct, a composite high-speed railway bridge. In Proc. 26th IMAC, International Modal Analysis Conference. 2008. p. 4–7.
[44] Peeters B, De Roeck G. Reference based stochastic subspace identification in civil engineering. Inverse Prob Eng 2000;8(1):47–74.
[45] Miyashita T, Ishii H, Fujino Y, Shoji T, Seki M. Understanding of high-speed-train-induced local vibration of a railway steel bridge using laser measurement and its effect by train speed. Doboku Gakkai Ronbunshuu A 2007;63(2):277–96. (In Japanese).
[46] Frýba L. Vibration of solids and structures under moving loads. Springer Science & Business Media. Vol. 1. 2013.
[47] Xia H, Zhang N, Guo WW. Analysis of resonance mechanism and conditions of train–bridge system. J Sound Vib 2006;297(3–5):810–22.
[48] Li J, Su M. The resonant vibration for a simply supported girder bridge under high-speed trains. J Sound Vib 1999;224(5):897–915.
[49] Adam C, Salcher P. Effect of the load modelling strategy on the dynamic response prediction of bridges subjected to high-speed trains. Dynamics and Control of Advanced Structures and Machines. Cham: Springer; 2017. p. 215–24.